



## Local-reconstruction enables cobalt phosphide array with bifunctional hydrogen evolution and hydrazine oxidation

Xiaotong Wei<sup>a,1</sup>, Shucong Zhang<sup>a,1</sup>, Xingshuai Lv<sup>b,1</sup>, Shuixing Dai<sup>a</sup>, Huanlei Wang<sup>a</sup>, Minghua Huang<sup>a,\*</sup>

<sup>a</sup> School of Materials Science and Engineering, Ocean University of China, Qingdao 266100, PR China

<sup>b</sup> Institute of Applied Physics and Materials Engineering, University of Macau, 999078, Macao Special Administrative Region of China



### ARTICLE INFO

#### Keywords:

Local reconstruction  
Hydrogen evolution  
Hydrazine electro-oxidation  
Transition metal phosphides  
Bifunctionality

### ABSTRACT

Coupling hydrazine electrooxidation with hydrogen evolution reaction (HER) attracts ever-growing attention for energy-saving H<sub>2</sub> production. However, the performance of hydrazine-assisted HER unit is restricted by the bifunctional catalysts with un-fully activated sites. Herein, a surface local-reconstruction strategy is proposed to integrate amorphous Co(OH)<sub>2</sub> and P vacant CoP into the CoH-CoPv@CFP catalyst. The inherent electron-deficient Co sites in Co(OH)<sub>2</sub> show strong N-Co interaction to accelerate the N<sub>2</sub>H<sub>4</sub> dehydrogenation kinetics, while the as-formed P vacancies in CoP play a crucial role in moderating the H<sup>\*</sup> adsorption energy, the excellent bifunctionality thus being obtained. Specifically, it achieves the low overpotentials of  $-77$  and  $-61$  mV at  $10$  mA cm<sup>-2</sup> for HER and HzOR in alkaline media, respectively. A lab-scale electrolyzer can deliver the industrial-grade current density of  $500$  mA cm<sup>-2</sup> under ultralow cell voltage of  $0.23$  V. This local-reconstruction strategy may pave new avenue to design efficient catalysts for hydrazine-assisted H<sub>2</sub> generation.

### 1. Introduction

Hydrogen receives a great deal of interest as appealing energy alternative for the conventional fossil fuels due to its high energy density and zero carbon emission nature [1–3]. Alkaline water electrolysis, involving the hydrogen evolution reaction (HER) at the cathode and oxygen evolution reaction (OER) at the anode, has been considered as an efficient and sustainable approach to generate high-purity hydrogen compared to the traditional steam reforming and coal gasification [4,5]. However, the sluggish OER ( $4\text{OH}^- = \text{O}_2 + 2\text{H}_2\text{O} + 4\text{e}^-$ ,  $1.23$  V vs. RHE) is especially restricted to the noble metal oxides (IrO<sub>2</sub> and RuO<sub>2</sub>) electrocatalysts with scarcity and high cost, which hinders the large-scale deployment of water electrolysis [6,7]. Noteworthy, the hydrazine oxidation reaction (HzOR,  $\text{N}_2\text{H}_4 + 4\text{OH}^- = \text{N}_2 + 4\text{H}_2\text{O}$ ,  $-0.33$  V vs. RHE) featured with the lowest thermodynamic potential attracts extensive attention as an appropriate alternative anodic reaction for energy-saving H<sub>2</sub> production [8,9]. Additionally, it enlightens an efficient way to fast remove hydrazine from industrial sewage without any Fenton reagent [10,11]. Considerable efforts have been devoted to exploiting advanced HzOR electrocatalysts based on earth-abundant

transition metal compounds, such as Ni<sub>2</sub>P, Ni<sub>3</sub>N and Co<sub>3</sub>N, etc, due to the tunable 3d electron structure and various chemical valence states for transition metals [12–15]. Whereas, the transition metal sites can also facilitate the fracture of N-N bond in N<sub>2</sub>H<sub>4</sub> molecule, leading to the formation of undesired NH<sub>3</sub> byproduct from the incomplete oxidation reaction [16]. Moreover, most reports have a tendency to exclusively optimize the performance for HzOR half-reaction, while the synergistic improvement of HER is being neglected. Consequently, it is urgent to design the transition metal based electrocatalysts, which enable the efficient N<sub>2</sub>H<sub>4</sub> activation and excellent bifunctionality for hydrazine-assisted H<sub>2</sub> generation.

Recently, transition metal phosphides (TMPs) have been proven to be the HER-preferred materials since the slightly electronegative P sites can readily attract the H<sup>+</sup> under alkaline condition featured in low proton concentration [17]. Unfortunately, these TMPs exhibits relatively inferior HzOR activity, which is caused by the sluggish adsorption kinetics of N<sub>2</sub>H<sub>4</sub> intermediates on nearly electroneutral metal sites, the bifunctionality thus being restricted [18]. It is generally acknowledged that the electron-deficient metal atom is the fundamental active sites towards HzOR [19]. The electron state regulation strategies (e.g., single atom

\* Corresponding author.

E-mail address: [huangminghua@ouc.edu.cn](mailto:huangminghua@ouc.edu.cn) (M. Huang).

<sup>1</sup> These authors contributed equally to this work.

engineering, heterostructure constructing, and etc.) have been currently utilized to facilitate surface charge redistribution for activating the surface HzOR-inert regions [20,21]. For example, single atom engineering can trigger the optimization of the electronic states around single atom sites by a strong metal-support interaction [22]. Heterojunction engineering has been widely reported to combine TMPs with other building blocks for achieving the interfacial electric field, where the electronic state reconfiguration occurs along the constructed heterointerface [23,24]. Despite the remarkable achievements in this field, the dilemma lie in that, on one hand, the optimized active sites are still plagued by insufficient electron delocalization, leading to the powerless adsorption ability. On the other hand, a large amount of metal sites that away from the modulation center are not fully activated due to the restricted extending distance of electron transfer, thus leading to unsatisfactory catalytic performance. Consequently, it is necessary to realize the full utilization of those silent metal sites by breaking or circumventing such inherent dynamical and spatial constraints of electron transfer. Surface reconstruction for TMPs has been performed to in-situ form the high-valence metal compounds (e.g. oxides, hydroxides, oxy-hydroxide) that possess the intrinsic electron-deficient metal sites, which are as highly active and stable species for oxidation reactions [25–27]. The reconstruction process usually occurs on the whole TMPs surface without clear distinction, which would no doubt help to accelerate HzOR kinetics, but probably at the risk of covering pristine HER active sites. Simultaneous consideration should be given to preserve the HER-preferred phosphide region while generating reconstructed the high-valence metal species, which in turn submits the demand on precise controllability of reconstruction engineering. Therefore, it is highly desirable to develop targeted-reconstruction to produce highly-efficient bifunctional catalysts toward HER and HzOR, however, this part has been less touched and remains vacant.

Herein, we propose a surface local-reconstruction strategy to in-situ transform the amorphous  $\text{Co(OH)}_2$  nanosheet from an incomplete phosphating CoP nanowires array, the electron deficient Co sites as HzOR sites and abundant P vacancies as HER centers thus being generated in the obtained  $\text{CoH-CoPv@CFP}$  catalyst. As expected, it can achieve the current densities of 10 and 100  $\text{mA cm}^{-2}$  at low overpotentials of  $-77$  and  $-130$  mV for HER in 1.0 M KOH solution. For HzOR, it only requires an ultralow working potential of  $-61$  and  $-45$  mV to reach 10 and 100  $\text{mA cm}^{-2}$  in 1.0 M KOH/0.4  $\text{N}_2\text{H}_4$  electrolyte. Furthermore, a lab-scale overall hydrazine splitting (OH<sub>2</sub>S) system using  $\text{CoH-CoPv@CFP}$  electrodes as bifunctional electrocatalysts requires a record-low cell voltage of 0.23 V can drive 500  $\text{mA cm}^{-2}$  with the outstanding stability, suggesting its industrial potential of energy-saving hydrogen production. The density function theory (DFT) calculation illustrates that electron-deficient Co sites in  $\text{Co(OH)}_2$  are identified as the HzOR centers by expressing more powerful N-Co interaction to accelerate  $\text{N}_2\text{H}_4$  dehydrogenation kinetics, while P vacancies in CoP could contribute to balancing the  $\text{H}^*$  adsorption/desorption for the superior HER activity. This work demonstrates that the surface local-construction could create the dual reactive sites towards HER and HzOR, and offers a general strategy for rationally designing the bifunctional catalysts.

## 2. Experimental section

### 2.1. Synthesis of $\text{CoCH-CoP@CFP}$

The target  $\text{CoCH-CoP@CFP}$  is fabricated via a hydrothermal and phosphorization process. Before the hydrothermal reaction, a piece of well-cut carbon fiber paper (CFP, 2.0 cm  $\times$  2.5 cm) is first ultrasonically cleaned with 3 M  $\text{H}_2\text{SO}_4$  (30 min), acetone (15 min), ethanol (15 min) and ultrapure water(5 min) in sequence to remove surface oxides. And the as-treated CFP was then transferred into a 20 mL Teflon lined autoclave containing the solution of  $\text{Co}(\text{NO}_3)_2 \cdot 6 \text{ H}_2\text{O}$  (1.164 g), urea (0.3 g) and  $\text{NH}_4\text{F}$  (0.074 g) and 20 mL deionized (DI) water, and hydrothermally reacted for 12 h at 120 °C. After cooling down to room

temperature, the pink Co precursors grown on CFP ( $\text{CoCH@CFP}$ ) was washed several times with DI water to remove the unreacted residues and fully dried under vacuum at 60 °C for 4 h. Subsequently, the  $\text{CoCH-CoP@CFP}$  is obtained by an incomplete phosphorylation process. Specifically, the  $\text{CoCH@CFP}$  and  $\text{NaH}_2\text{PO}_2$  (0.25 g) were placed in two ceramic boats located downstream and upstream of the tube furnace, respectively. The phosphating process was carried out at a temperature of 300 °C for 20 min with a heating rate of 10 °C min<sup>-1</sup> under high-purity Ar atmosphere.

### 2.2. Synthesis of $\text{CoH-CoPv@CFP}$

The  $\text{CoH-CoPv@CFP}$  was obtained by a reconstruction process for the as-synthesized  $\text{CoCH-CoP@CFP}$  using the strong reducing  $\text{NaBH}_4$  solution. Specifically,  $\text{CoCH-CoP@CFP}$  was immersed in a beaker containing  $\text{NaBH}_4$  (3 M) solution for 0.5 h. The target  $\text{CoH-CoPv@CFP}$  was obtained after being washed for several times with deionized water.

### 2.3. Physical characterizations

X-ray powder diffraction (XRD) patterns are acquired on the Rigaku Ultima IV diffractometer. The scanning electron microscopy (SEM) images are implemented on the: ZEISS Gemini 300 field emission electron microscope. The transmission electron microscopy (TEM) and high-resolution transmission electron microscopy (HRTEM) are performed on the FEI TalosF200x. Inductively coupled plasma optical emission spectrometry (ICP-OES) measurement is performed by Thermo Fisher iCAP PRO. The X-ray photoelectron spectroscopy (XPS) is carried out on the Thermo Fisher ESCALAB XI+. The Raman spectra are implemented on the HORIBA scientific Lab RAM HR evolution high resolution Raman spectrometer. The Electron paramagnetic resonance (EPR) spectroscopy is tested using Bruker EMXplus-6/1 spectrograph. Kelvin Probe force microscopy (KPFM) is employed to measure the surface potential of catalysts. X-ray absorption spectra (XAS) including X-ray absorption near-edge structure (XANES) and extended X-ray absorption fine structure (EXAFS) at Co K-edge of the samples are recorded at the beamline BL14W1 of Shanghai Synchrotron Radiation Facility (SSRF) in China.

### 2.4. Electrochemical measurements

All electrochemical performance of the catalysts is measured on a typical three-electrode cell using the Biologic SP-300 (France) electrochemical workstation. The synthesized catalysts were used as working electrodes, graphite rods and saturated  $\text{Hg}/\text{HgO}$  electrodes as auxiliary and reference electrodes, respectively. All the recorded potentials are calibrated to the reversible hydrogen electrode (RHE) by using the following equation:  $E_{(\text{RHE})} = E_{(\text{Hg}/\text{HgO})} + 0.098 \text{ V} + 0.059 \text{ pH}$ . The polarization curves corrected with 80% iR compensation are measured at a scan rate of 5  $\text{mV s}^{-1}$ . The Tafel slope is obtained by Tafel equation [ $\eta = \text{blog}(j) + a$ ]. Electrochemical impedance spectroscopy (EIS) measurements are performed in a frequency range from 0.01 Hz to  $10^5$  Hz. The double-layer capacitance ( $C_{dl}$ ) of the investigated catalysts is estimated by employing cyclic voltammetry (CV) in a non-Faradaic area with different scan rates. The turnover frequency (TOF) values are calculated by the following equation:  $\text{TOF} = \frac{|j|A}{mF}$ , where  $|j|$  refers to the current density at a constant potential during the LSV measurement. A stand for the electrode area and F is the Faradaic constant ( $96485 \text{ C mol}^{-1}$ ). m represents the electrons transfer numbers during HzOR or HER process. n is the number of active sites.

### 2.5. Computational methods

The spin-polarized density functional theory (DFT) calculations were performed using the projected augmented wave (PAW)

pseudopotentials and Perdew-Burke-Ernzerhof generalized gradient exchange-correlational functional as implemented in the Vienna ab-initio Simulation Package (VASP). The cut-off energy was set to 450 eV and the convergence threshold was set to  $10^{-5}$  in energy and 0.02 eV/Å in force. The van der Waals (vdW) interactions between catalysts and reaction species were treated using the Grimme's D3-type of the semiempirical method. The Brillouin zone was sampled by a Monkhorst-Pack k-point mesh of  $5 \times 5 \times 1$  grid, and a vacuum layer of 15 Å was employed to avoid interactions of neighboring images.

### 3. Results and discussion

#### 3.1. Synthesis and characterization

The fabrication process of hierarchical  $\text{Co(OH)}_2$  sheets-Co $\text{P}_\text{V}$  nanowires grown on carbon fiber paper (CoH-Co $\text{P}_\text{V}$ @CFP) is illustrated in Fig. 1a. We elaborately construct the metastable  $\text{Co}_6(\text{CO}_3)_2(\text{OH})_8 \cdot \text{H}_2\text{O}$  (CoCH) nanowires grown on carbon fiber paper (CoCH@CFP) as catalyst precursor to trigger the surface local-reconstruction (Fig. S1). The CoCH precursor is then subjected to an incomplete phosphorization, achieving a coexistence of CoCH and newly formed CoP phase to form CoCH-CoP@CFP. Subsequently, a local-reconstruction on CoCH-CoP@CFP surface is triggered to generate target CoH-Co $\text{P}_\text{V}$ @CFP catalyst by performing  $\text{NaBH}_4$  reduction treatment, in which the CoCH is transformed into amorphous  $\text{Co(OH)}_2$  nanosheet. The deliberate choice of metastable CoCH species is based on the following consideration. The metastable CoCH species involving one-dimensional chain-like crystal structure unit and the inserted  $\text{CO}_3^{2-}$  ion interlayers between  $\text{M(OH)}_6$  octahedra layers, featured with high-energy structure and high reactivity surface exhibit the thermodynamic instability property, is prone to be transformed into the relatively stable hydroxide counterpart under strong reduction conditions [28–30]. X-ray diffraction (XRD) measurement is

employed for exploring the detailed phase and crystal structure of the as-synthesized samples (Fig. 1b). As can be seen, the diffraction peaks of CoCH-CoP@CFP at  $30.5^\circ$ ,  $33.9^\circ$ ,  $36.5^\circ$ ,  $39.6^\circ$ ,  $47.2^\circ$ ,  $54.1^\circ$ ,  $56.0^\circ$ ,  $59.7^\circ$  and  $62.1^\circ$  are well matched with the  $\text{Co}_6(\text{CO}_3)_2(\text{OH})_8 \cdot \text{H}_2\text{O}$  (PDF #48-0083), [28] and the other characteristic peaks can be indexed to CoP (PDF #29-0497), which confirms the coexistence of CoCH and CoP phases in the CoCH-CoP@CFP. After local reconstruction for CoH-Co $\text{P}_\text{V}$ @CFP, the peaks related to CoCH completely disappear, suggesting that CoCH crystalline phase maybe selectively reconstructed into an amorphous form. The retaining ones centered at  $31.6^\circ$ ,  $35.2^\circ$ ,  $36.3^\circ$ ,  $46.2^\circ$ ,  $48.1^\circ$ ,  $48.4^\circ$ ,  $52.2^\circ$ ,  $56.3^\circ$  and  $56.8^\circ$  correspond to the (011), (200), (111), (112), (211), (202), (103), (212), and (301) crystal planes of CoP, indicating that the CoP crystalline phase are well reserved. This result can be further evidenced by Raman spectra (Fig. S2), where the peaks at around  $468.8$ ,  $512.2$ , and  $674.5 \text{ cm}^{-1}$  are assigned to  $\text{E}_g$ ,  $\text{F}_{2g}$ , and  $\text{A}_{1g}$  vibration modes of CoP, can be observed for CoCH-CoP@CFP [31]. These characteristic Raman peaks show obvious red-shift for the CoH-Co $\text{P}_\text{V}$ @CFP, which may be caused by change of surface strain during reconstruction process, illustrating that the  $\text{NaBH}_4$  with strong reducibility can attack the Co-P bond and create abundant P vacancies in CoP phase [32,33]. In response, the electron paramagnetic resonance (EPR) is adopted to explore the existence and the concentration of vacancies in CoH-Co $\text{P}_\text{V}$ @CFP, and the results are shown in Fig. S3. As expected, an increased symmetrical EPR signal appears at  $g = 2.04$  relative to the original CoCH-CoP@CFP, which could be assigned to the generation of paramagnetic P vacancies. As known, the abundant vacancies usually play an important role in enhancing the electrocatalytic performance [34].

The morphological characterizations of the as-obtained catalysts are performed by scanning electron microscopy (SEM) and transmission electron microscopy (TEM). As shown in Fig. S4a and S4b, the CoCH nanowire array grown densely and evenly on the CFP can be observed

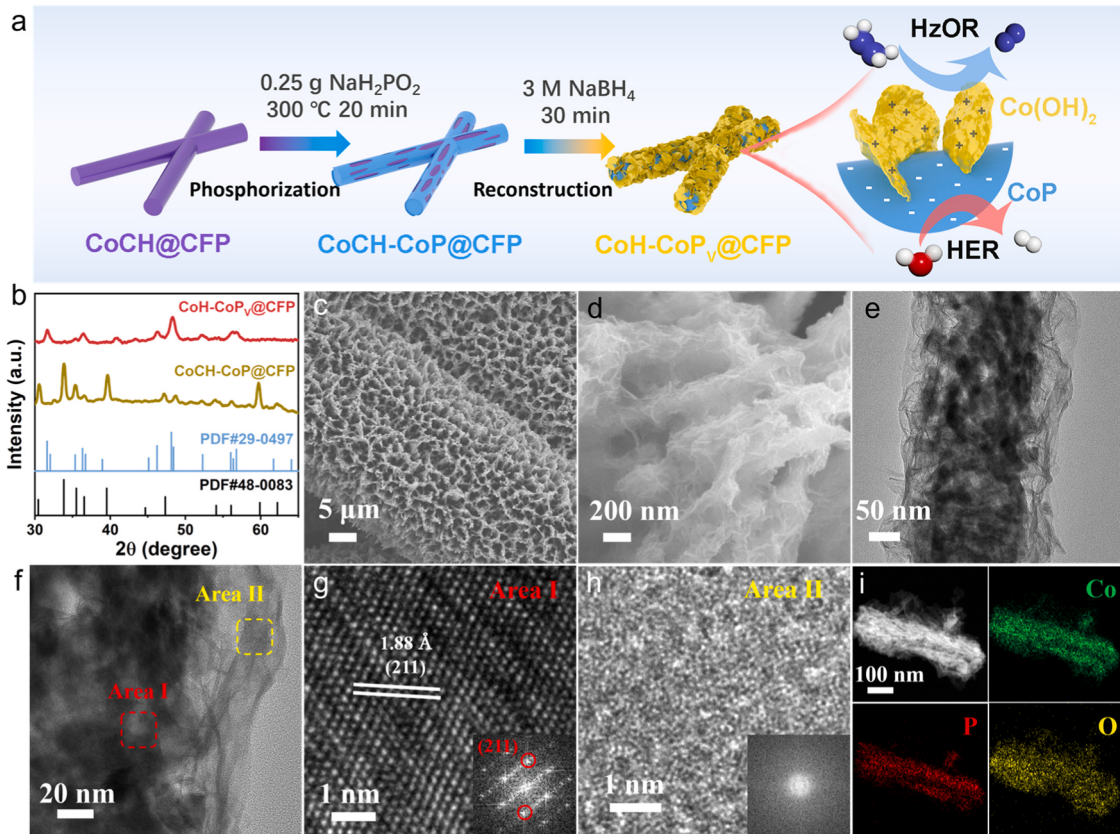


**Fig. 1.** (a) Schematic illustration for the fabrication of CoH-Co $\text{P}_\text{V}$ @CFP catalyst. (b) XRD pattern of CoH-Co $\text{P}_\text{V}$ @CFP and CoCH-CoP@CFP. (c, d) SEM images. (e) TEM image. (f-h) HRTEM images of CoH-Co $\text{P}_\text{V}$ @CFP. (i) Elemental mapping spectrum of Co, P, O elements.

for CoCH@CFP. After phosphorization process, the obtained CoCH-CoP@CFP is almost consistent with the former in size and morphology (Fig. S4c and S4d). Impressively, a significant morphology change occurs on the surface of target CoH-CoPv@CFP (Figs. 1c and 1d). The interconnected and flexible nanosheets are wrapped with the nanowires and a hierarchical architecture is thus generated, which may be conducive to the full exposure of active sites and mass transport during electrochemical reaction process [35]. In response, the contact angle tests are adopted to investigate the wettability of the catalysts. As shown in Fig. S5, the CoH-CoPv@CFP shows a near 0° of water contact angle (CA), suggesting its superhydrophilic property. In contrast, the CAs of bare CFP and CoCH-CoP@CFP are measured to be as large as 125.6° and 8.5°, respectively. Additionally, the aerophobic property of the catalysts is investigated by measuring the CAs of the air bubbles in the water. The bubble CA of the CoH-CoPv@CFP is measured to be 156.6°, which is larger than those of the bare CFP (118.9°) and CoCH-CoP@CFP (135.3°), indicating that the CoH-CoPv@CFP possesses the minimized

gas-liquid contact area for accelerating the bubble detachment. The nanowires interwoven with typical stacked and staggered ultrathin nanosheets can be further revealed in TEM images (Figs. 1e and S6), implying potential porous configuration and abundant infiltration gap, which is consistent with SEM results [36]. High-resolution TEM (HR-TEM) images display the lattice fringe spacings of 1.88 Å in area I for the inner nanowires, which is attached to (111) plane of standard CoP, confirming the successful reserve of CoP crystalline phase during reconstruction (Figs. 1f and 1g). Meanwhile, no obvious lattice stripes could be observed in the area II for the surficial nanosheets, manifesting its amorphous nature (Fig. 1h). Afterwards, heterogeneous distribution of P, Co and O elements in CoH-CoPv@CFP are shown by elemental mappings in Fig. 1i. The P and O signals are separately detected in nanowires and nanosheets, whilst the Co atoms are uniformly distributed throughout the whole system. The P and Co contents are determined to be 12.4 wt% and 70 wt% in CoH-CoPv@CFP by inductively coupled plasma optical emission spectrometry (ICP-OES), indicating

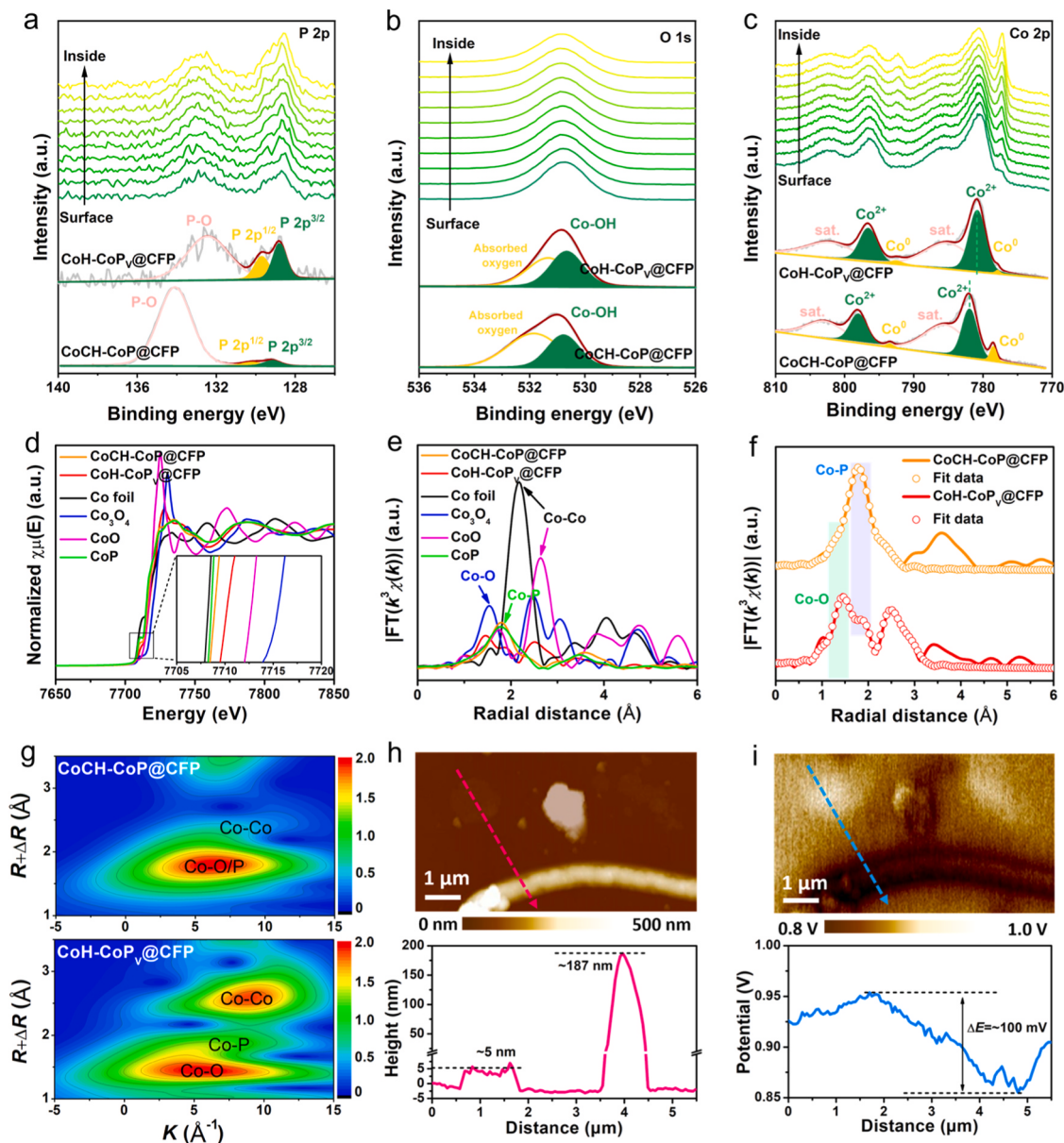


**Fig. 2.** High-resolution XPS spectra and XPS depth profile of (a) P 2p, (b) O 1s and (c) Co 2p. (d) Co K-edge XANES spectra. (e) Co K-edge FT-EXAFS spectra for CoH-CoPv@CFP, CoCH-CoP@CFP, Co foil,  $\text{Co}_3\text{O}_4$ , CoO and CoP. (f) The corresponding fitting curves of CoH-CoPv@CFP and CoCH-CoP@CFP. (g) Wavelet transform for the  $k^3$ -weighted EXAFS signals of CoH-CoPv@CFP and CoCH-CoP@CFP. (h) AFM image and (i) KPFM image of CoH-CoPv@CFP.

that the ratio of CoP and  $\text{Co(OH)}_2$  may be 1:4.6 (Table S1).

X-ray photoelectron spectroscopy (XPS) was conducted to investigate the chemical composition of the samples. In the P 2p spectrum of  $\text{CoH-CoPy@CFP}$  (Fig. 2a), two peaks of phosphide species at 129.7 (P 2p<sub>1/2</sub>) and 128.8 eV (P 2p<sub>3/2</sub>) exhibit a significant increase in intensity compared to the  $\text{CoCH-CoP@CFP}$ , while the P-O peak representing phosphate at 132.4 eV decreases for  $\text{CoH-CoPy@CFP}$ . These results mean that some phosphate may be reduced into metallic P during local-reconstruction process. In the O 1 s spectrum (Fig. 2b), the peaks located at 530.6 eV for  $\text{CoH-CoPy@CFP}$  refers to the hydroxide group. As shown in Fig. 2c, the Co 2p spectrum of  $\text{CoCH-CoP@CFP}$  can be deconvoluted into two fitting peaks located at 798.0 and 781.9 eV, respectively, which are attributed to the  $\text{Co}^{2+}$  in  $\text{CoCH}$  species [37]. Compared to  $\text{CoCH-CoP@CFP}$ , the  $\text{Co}^{2+}$  peaks shift to lower binding energy with an increased intensity for the obtained  $\text{CoH-CoPy@CFP}$  after local-reconstruction, indicating the increased valance state of Co [36, 38]. The other two peaks at 793.5 and 778.4 eV are assigned to  $\text{Co}^0$  for both  $\text{CoCH-CoP@CFP}$  and  $\text{CoH-CoPy@CFP}$ , indicating the formation of Co-P bonding [39]. It is worth noting that the signals of  $\text{Co}^0$  peak decrease after the reconstruction. It is possible that the CoP are covered by the Co hydroxide nanosheets transformed from  $\text{CoCH}$  in the reconstruction process. To make the exposure of internal CoP, etching XPS spectra with Ar plasma are therefore conducted to remove the surface Co hydroxide. With the etching time from 0 to 200 s, the intensity of  $\text{Co}^{2+}$  and  $\text{OH}^-$  peaks gradually decline in Co 2p and O 1 s spectra, which indicates the successful removal of surface Co hydroxide sheets. In contrast, the peaks of  $\text{Co}^0$  increase continuously, illustrating that abundant CoP species indeed exist in the inner nanowires, which can be further confirmed by the gradually enhanced metallic P signals in etching P 2p XPS spectrum [40]. The depth profile results indicate the co-existence of inner CoP and outer  $\text{Co(OH)}_2$  species in the  $\text{CoH-CoPy@CFP}$ , in line with the TEM results.

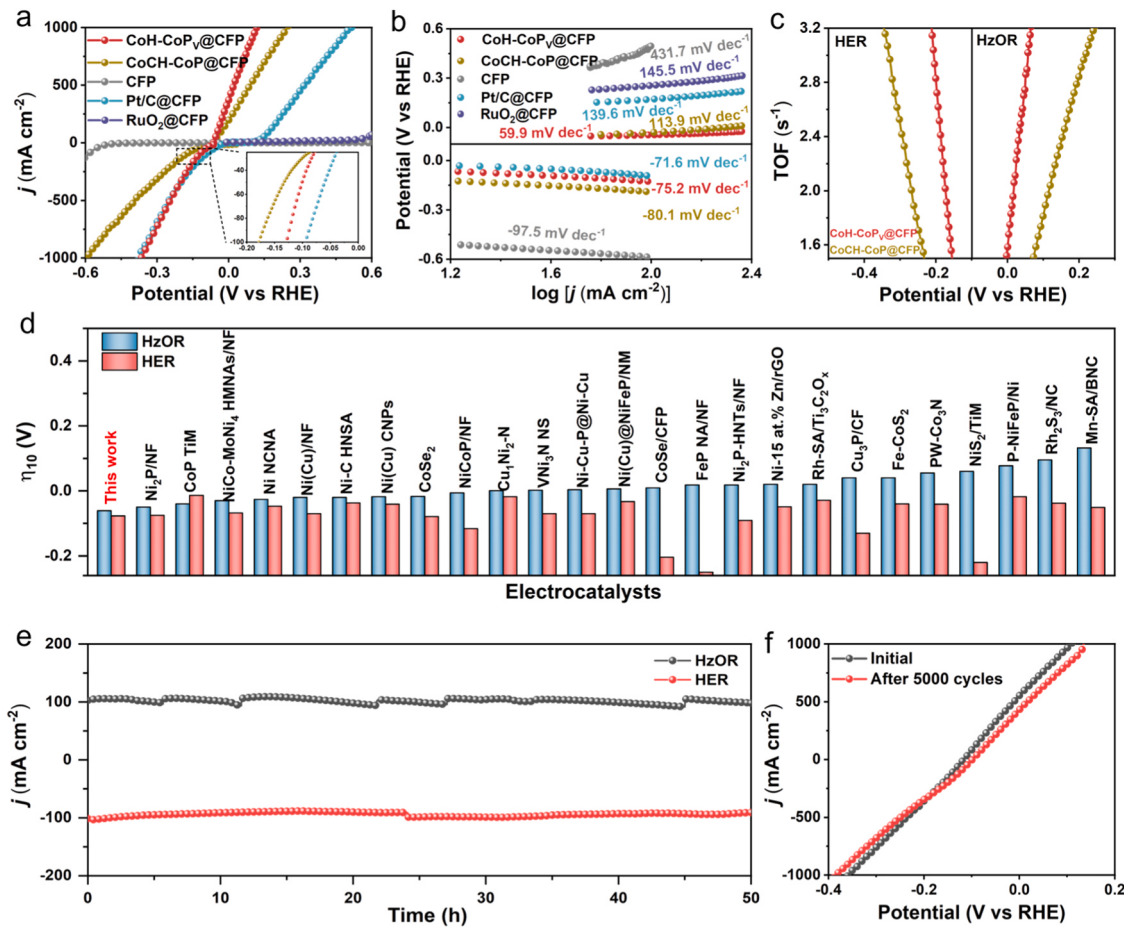
The local electronic states and coordination structures of the as-prepared catalysts are investigated by X-ray absorption fine-structure (XAFS) spectroscopy. The Co K-edge X-ray absorption near-edge structure (XANES) spectra show that the absorption edges of Co for both  $\text{CoCH-CoP@CFP}$  and  $\text{CoH-CoPy@CFP}$  are located between that of Co foil and  $\text{CoO}$ , suggesting their average valances are in the range from 0 to + 2 (Fig. 2d). Meanwhile, the Co valance state in  $\text{CoCH-CoP@CFP}$  is higher than standard CoP, which suggests that the co-existence of CoP and  $\text{CoCH}$  increase the average Co valance in  $\text{CoCH-CoP@CFP}$ . Notably, the Co absorption edge in  $\text{CoH-CoPy@CFP}$  shifts toward higher energy compared to that in  $\text{CoCH-CoP@CFP}$ , indicating the higher average oxidation state of Co in the former than that in the latter [41]. Fig. 2e shows the Fourier transformed k2-weighted  $\chi(k)$ -function of extended X-ray absorption fine structure (FT-EXAFS) spectra. Two scattering peaks are located at  $\approx 1.8\text{--}1.9\text{ \AA}$  for  $\text{CoCH-CoP@CFP}$  and  $\text{CoH-CoPy@CFP}$ , which are ascribed to the scattering paths of Co binding with P. The Co-O peak at  $1.46\text{ \AA}$  for  $\text{CoH-CoPy@CFP}$  exhibits a higher intensity relative to  $\text{CoCH-CoP@CFP}$ , illustrating that the successful transformation of  $\text{Co(OH)}_2$  species [42]. The local coordination structure feature of Co is identified by fitting the EXAFS results (Fig. 2f and Fig. S7). As summarized in Table S2, the coordination numbers of Co-P and Co-O in  $\text{CoH-CoPy@CFP}$  are fitted as 2.1 and 3.0, respectively, which has a lower ratio (2:3) than that in  $\text{CoCH-CoP@CFP}$  (1:1), further suggesting the increased oxidation state of Co during reconstruction process. The Co K-edge FT-EXAFS spectrum in K space declares that the oscillation trend of  $\text{CoH-CoPy@CFP}$  is close to those of both  $\text{CoCH-CoP@CFP}$  and standard CoP between 0 and  $6\text{ \AA}^{-1}$  (Fig. S8), manifesting that the main Co-P coordination is well-preserved in the  $\text{CoH-CoPy@CFP}$  [43]. The wavelet transformed Co K-edge EXAFS spectrum (Fig. 2g and S9) of  $\text{CoCH-CoP@CFP}$  shows the contour intensity maximum at  $\sim 6.2\text{ \AA}^{-1}$ , representing the coordination of Co-P/O. Two obvious signals of Co-P ( $\sim 6.6\text{ \AA}^{-1}$ ) and Co-O ( $\sim 5.5\text{ \AA}^{-1}$ ) can be clearly observed for  $\text{CoH-CoPy@CFP}$ , implying the co-existence of CoP and  $\text{Co(OH)}_2$  on the catalyst surface. The atom force microscopy (AFM)

image shows that the  $\text{Co(OH)}_2$  sheet in thickness of around 5 nm and CoP rod in diameter of about 187 nm (Figs. 2h and 2i). In addition, the surface potentials of the  $\text{Co(OH)}_2$  and CoP areas are visualized by the Kelvin probe force microscopy (KPFM) measurement [44]. The surface potential of the  $\text{Co(OH)}_2$  sheet is determined to be  $\sim 0.96$  V, which is about 100 mV higher than that of CoP, implying more positive charge is distributed on the surface of  $\text{Co(OH)}_2$  than that of CoP. Such positively charged  $\text{Co(OH)}_2$  is expected to offer abundant active sites for improving the HzOR activity, while the relatively negative CoP can act as the efficient active center for catalyzing HER.

### 3.2. Evaluation of electrocatalytic HER and HzOR performance

The HER and HzOR performance of the  $\text{CoH-CoPy@CFP}$  has been measured in 1.0 M KOH solution using a typical three-electrode system, and the  $\text{CoCH-CoP@CFP}$ , bare CFP, and commercial Pt/C and  $\text{RuO}_2$  catalysts loaded on CFP substrate (Pt/C@CFP and  $\text{RuO}_2$  @CFP) are also measured as controls. Fig. 3a shows the linear sweep voltammetry (LSV) curves for those catalysts. As can be seen, the  $\text{CoH-CoPy@CFP}$  shows a high HER activity, in which the overpotentials of  $-77$  and  $-130$  mV are required to obtain the current densities of 10 and  $100\text{ mA cm}^{-2}$ , surpassing those of  $\text{CoCH-CoP@CFP}$  ( $-101$  and  $-191$  mV), Pt/C@CFP ( $-27$  and  $-98$  mV), and bare CFP. For the HzOR, 1.0 M KOH + 0.4 M  $\text{N}_2\text{H}_4$  solution is selected to be as the electrolyte (Fig. S10). The  $\text{CoH-CoPy@CFP}$  presents the HzOR potentials of merely  $-61$  and  $-45$  mV for achieving 10 and  $100\text{ mA cm}^{-2}$  current densities, lower than that of  $\text{CoCH-CoP@CFP}$  ( $-56$  and  $-26$  mV), Pt/C@CFP (115 and 172 mV),  $\text{RuO}_2$ /CFP and bare CFP. Moreover, the  $\text{CoH-CoPy@CFP}$  also exhibits the remarkable electrocatalytic activity under high current density, where  $1000\text{ mA cm}^{-2}$  can be obtained with the overpotentials of 367 and 117 mV for HER and HzOR, respectively, implying its potential for industrial application. Fig. S11 gives the LSV comparison between HzOR and OER for  $\text{CoH-CoPy@CFP}$ . The potential reductions of 1.62 and 1.65 V occur in HzOR relative to OER for reaching 100 and  $500\text{ mA cm}^{-2}$  current densities, suggesting that replacing OER with HzOR to couple HER for hydrogen production can significantly reduce energy consumption [45]. For HzOR, there are negligible changes in current density during the LSV scanning process (varied rates from 5 to  $100\text{ mV s}^{-1}$ ), suggesting the efficient charge and mass transfer at the catalyst-liquid-gas three-phase interface for  $\text{CoH-CoPy@CFP}$  (Fig. S12) [7].

The Tafel slope calculation has been performed to investigate the reaction kinetics of all catalysts. As presented in Fig. 3b, the  $\text{CoH-CoPy@CFP}$  has the smallest Tafel slopes of  $-75.2\text{ mV dec}^{-1}$  for HER and  $59.9\text{ mV dec}^{-1}$  for HzOR compared to the  $\text{CoCH-CoP@CFP}$  ( $-80.1$  and  $113.9\text{ mV dec}^{-1}$ ), CFP ( $-97.5$  and  $431.70\text{ mV dec}^{-1}$ ), Pt/C@CFP ( $-71.6$  and  $139.6\text{ mV dec}^{-1}$ ) and  $\text{RuO}_2$ /CFP ( $145.5\text{ mV dec}^{-1}$  for HzOR) indicating that the fastest HER and HzOR kinetics for  $\text{CoH-CoPy@CFP}$ . The electrochemical impedance spectroscopy (EIS) measurement under different voltages displays that the  $\text{CoH-CoPy@CFP}$  has a lower charge transfer resistance ( $R_{ct}$ ) than  $\text{CoCH-CoP@CFP}$  under each voltage for both HER and HzOR, suggesting the accelerated charge transfer rate for the former (Fig. S13). It is worth mentioning that the  $\text{CoH-CoPy@CFP}$  possesses the higher  $C_{dl}$  values of  $112.7$  and  $68.5\text{ mF cm}^{-2}$  for HER and HzOR than  $\text{CoCH-CoP@CFP}$  ( $92.0$  and  $62.1\text{ mF cm}^{-2}$ ), confirming more exposure of active sites on the  $\text{CoH-CoPy@CFP}$  surface (Fig. S14). The corresponding normalized LSV curves could indicate the enhanced intrinsic HER and HzOR activities for  $\text{CoH-CoPy@CFP}$  (Fig. S15). The high intrinsic activity for  $\text{CoH-CoPy@CFP}$  can be further confirmed by the larger TOF values than  $\text{CoCH-CoP@CFP}$ , shown in Fig. 3c. Getting benefits from many advantageous factors, such as the fast reaction kinetics, rapid charge transfer rate, abundant active sites and improved inherent activities, the  $\text{CoH-CoPy@CFP}$  exhibits the comparable HER and HzOR performance to the most reported non-noble metal-based catalysts (Fig. 3d and Table S3). The stability is also one of the key indicators to evaluate the performance of the catalysts. The evidence of



**Fig. 3.** (a) LSV curves, and (b) corresponding Tafel plots of CoH-CoPy@CFP, CoCH-CoP@CFP, CFP and Pt/C@CFP for HER and HzOR. (c) TOF values for CoH-CoPy@CFP, CoCH-CoP@CFP. (d) Comparison of CoH-CoPy@CFP with the recently reported catalysts at 10 mA cm<sup>-2</sup> for HER and HzOR. (e) The chronoamperometric curve, and (f) LSV curves before and after 5000 cycles for CoH-CoPy@CFP.

excellent long-term stability for CoH-CoPy@CFP can be found in result of the chronoamperometric test. As shown in Fig. 3e, the current density of 100 mA cm<sup>-2</sup> can be well retained for HER and HzOR, which only has about 2% and 5% decay in current density at the end of 50 h, respectively. In addition, the LSV curves of CoH-CoPy@CFP show no significant shift compared to the initial ones after 5000 cycles, indicating its wonderful cycling stability (Fig. 3f). From the XRD patterns and SEM images (Fig. S16a-e) after cycling stability, the nanowires array, composition, and crystal structure of the catalyst have been well preserved, while a slight decrease in P vacancy concentration can be observed in the EPR results (Fig. S16f). Meanwhile, valence state of the elements also remains almost unchanged according to the XPS spectra, illustrating the excellent stability (Fig. S16g-l).

### 3.3. Theoretical calculation

Density functional theory (DFT) calculation is performed to deeply reveal the underlying mechanism for the promoted HER and HzOR. As shown in Fig. 4a, the structural models and corresponding charge density difference plots of Co(OH)<sub>2</sub>, CoP and P-vacant CoP (CoPy) are deliberately simulated. As can be seen, the electron is mainly distributed around the O atoms for Co(OH)<sub>2</sub>, thus resulting in the electron deficient Co atoms, which may act as the active sites for efficiently catalyzing HzOR. For the CoP, the electron cloud on Co atoms is attracted by the neighbor P atoms and shifts to the latter, forming the charge accumulation on P. After removing one of the neighbor P to produce CoPy, the equilibrium state of charge distribution on Co atom is broken, and more electrons concentrate on the other adjacent P atoms. As reported, the

electron-rich P sites could be conducive to the H<sup>\*</sup> adsorption for improving the intrinsic HER activity [18]. Furthermore, the density of states (DOS) calculation is further adopted to explore the H<sup>\*</sup> adsorption on the catalyst surface. Fig. 4b manifests that the Co 3d orbitals makes main contribution to the total DOS of Co(OH)<sub>2</sub>, CoP, and CoPy near the Fermi level (E<sub>F</sub>). The d-band center (E<sub>d</sub>) is used to be as the descriptor to investigate the binding strength of reaction intermediates on the catalyst surface [46]. The E<sub>d</sub> of the CoPy (−1.43 eV) is between those of the CoP (−1.39 eV) and Co(OH)<sub>2</sub> (−1.45 eV), which illustrates that the CoPy has a moderate adsorption of intermediates on the surface [39]. The free energies of the dehydrogenation process for HzOR and the H<sup>\*</sup> adsorption/desorption kinetics for HER are also investigated. It is known that intrinsic HzOR activity is usually determined by the most endothermic dehydrogenation step, which represents the rate-determining step (RDS) for the whole HzOR process (Figs. 4c and S17) [47]. The RDS for Co(OH)<sub>2</sub> is the first dehydrogenation (\*N<sub>2</sub>H<sub>4</sub> → \*N<sub>2</sub>H<sub>3</sub>), and the corresponding free energy difference (ΔG) is calculated to be 0.59 eV. For the CoP, the RDS is the second dehydrogenation from \*N<sub>2</sub>H<sub>3</sub> to \*N<sub>2</sub>H<sub>2</sub>, and the corresponding energy barrier is as high as 0.72 eV. These results reveal that the HzOR may prefer to occur on the Co(OH)<sub>2</sub>, in which the electron-deficient Co sites act as the active centers. The free energy of hydrogen absorption (ΔG<sub>H\*</sub>) as the critical descriptor has been generally utilized to evaluate the HER intrinsic activity, where the thermoneutral free energy (ΔG<sub>H\*</sub> ≈ 0) represent the favorable adsorption [48,49]. As presented in Figs. 4d and S18, ΔG<sub>H\*</sub> of Co(OH)<sub>2</sub> is calculated to be 1.85 eV, which suggests the too weak binding strength for H<sup>\*</sup> on the catalyst surface. For the CoP, it possesses a ΔG<sub>H\*</sub> of −0.37 eV on the P sites, which is lower than that of Co(OH)<sub>2</sub>.

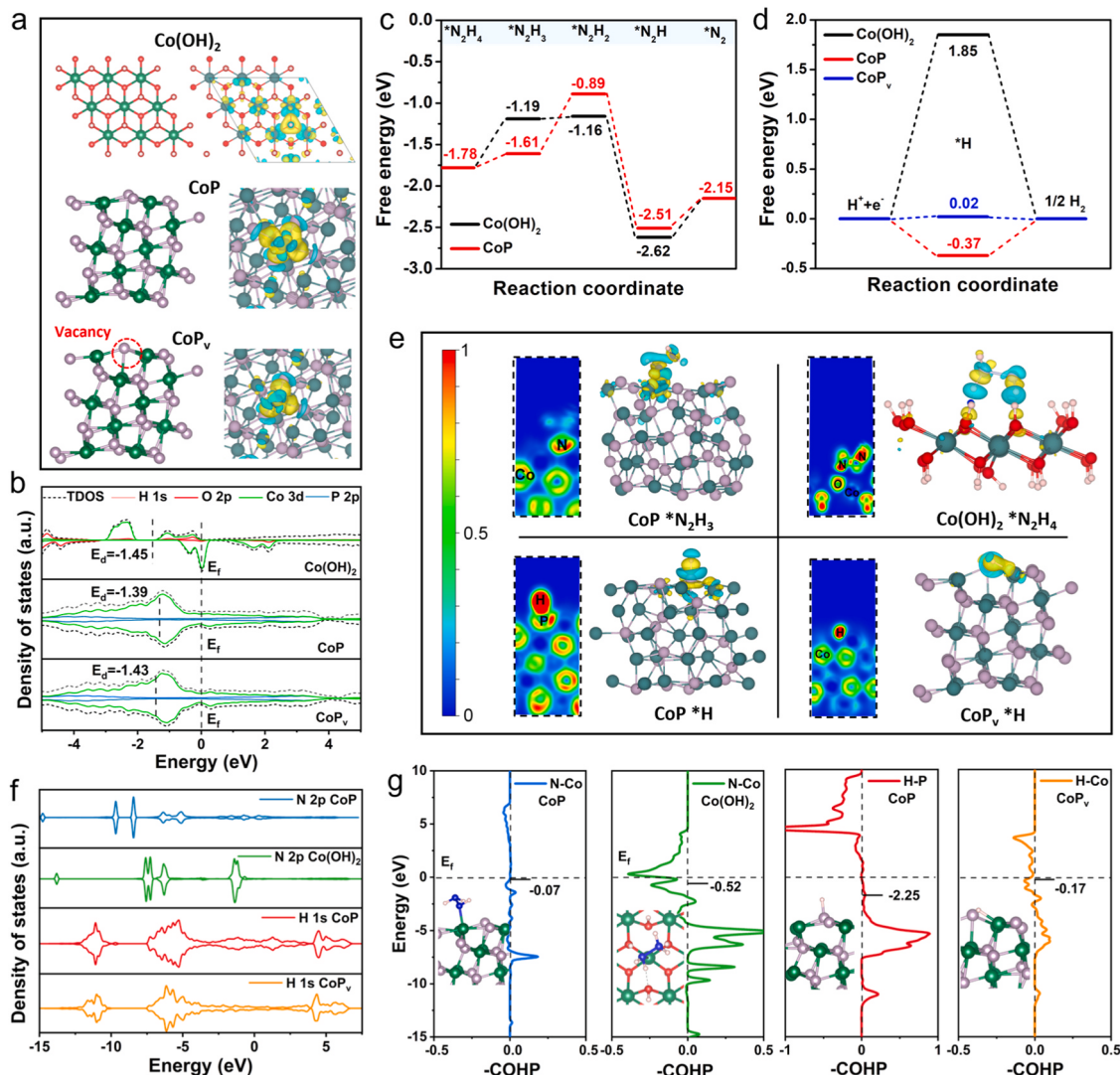


**Fig. 4.** (a) Charge density difference, and (b) DOS curves of Co(OH)<sub>2</sub>, CoP and CoP<sub>v</sub>. (c) Reaction pathways in the HzOR process for Co(OH)<sub>2</sub> and CoP. (d) Free energy diagram for H\* adsorption on Co(OH)<sub>2</sub>, CoP and CoP<sub>v</sub>. (e) Charge density difference and ELF evaluation, (f) PDOS curves, and COHP curves for the HER and HzOR intermediates adsorption on Co(OH)<sub>2</sub>, CoP and CoP<sub>v</sub>.

After introducing the P vacancy into CoP, the adsorption sites are changed into the Co sites for CoP<sub>v</sub>. The corresponding  $\Delta G_{H^*}$  is increased to be 0.02 eV, close to a thermoneutral value of 0 eV. The free energy analysis indicates that Co(OH)<sub>2</sub> and CoP<sub>v</sub> are as the HzOR and HER centers, respectively, and the integration of which could possess the favorable reaction kinetics to endow the bifunctionality for the catalyst.

The electron interplay between active sites and intermediates is visualized by the charge density difference and the electron localization function (ELF) diagrams to uncover the promotion mechanism of the catalysts (Fig. 4e). For HzOR, the \*N<sub>2</sub>H<sub>3</sub> intermediate in RDS of CoP (\*N<sub>2</sub>H<sub>3</sub> → \*N<sub>2</sub>H<sub>2</sub>) is adsorbed on the surface and exhibits the electron transfer from N to Co. Interestingly, such electron behavior in Co(OH)<sub>2</sub> (RDS, \*N<sub>2</sub>H<sub>4</sub> → \*N<sub>2</sub>H<sub>3</sub>) is switched into dual-site electron interaction, in which two N atoms in \*N<sub>2</sub>H<sub>4</sub> are captured by the surficial Co sites with the electron flow from the former to the latter. Therefore, the enhanced HzOR kinetics of Co(OH)<sub>2</sub> may be attributed to the formation of dual-site electron interaction, which is conducive to the electron transfer between active sites and intermediates, thus promoting the dehydrogenation process. For HER, the H\* intermediate adsorbs on the CoP surface via a powerful P-H bonding and captures electrons from the P atoms, thus leading to a relatively strong binding strength. Upon the introduction of the P vacancy into CoP, the adsorption sites for H\* on the

CoP<sub>v</sub> is switched into Co atoms, the binding force of H\* on the catalyst surface are thus weakened to a certain extent. As a result, the  $\Delta G_{H^*}$  of the CoP<sub>v</sub> could be up-shifted towards the zero value, which is in favor of the enhancement of HER activity. The projected DOS (PDOS) is also performed to explore the electron interaction between the intermediates and active sites. As shown in Fig. 4f, both of CoP and Co(OH)<sub>2</sub> present the p-d overlaps between the N 2p orbital in hydrazine intermediates (\*N<sub>2</sub>H<sub>3</sub> and \*N<sub>2</sub>H<sub>4</sub>) and the Co 3d orbital in Co atoms for HzOR process, in which the electron states of N 2p in the Co(OH)<sub>2</sub> exhibits a higher occupation than that in the CoP below the Fermi level, illustrating the stronger orbital interaction [50]. For HER, a minor decrease in electron states occupation of the H 1s orbitals can be observed in CoP<sub>v</sub> as introducing the P vacancy into the CoP, meaning the slight decrease in adsorption strength of H\* on the CoP<sub>v</sub> surface [51]. Furthermore, a crystal orbital Hamilton population (COHP) was used to theoretically analyze the bonding interaction between intermediates and catalyst surface (Fig. 4g). The higher occupied antibonding states for Co(OH)<sub>2</sub> near the Fermi level manifests the stronger hybridization between the Co 3d and N 2p orbital, which ensures the N<sub>2</sub>H<sub>4</sub> adsorption on catalyst surface [52]. The Co-N bond strength is quantified by the integrated COHP (ICOHP). Compared to that of CoP (0.07 eV), the larger value of 0.52 eV for Co(OH)<sub>2</sub> reveals the promoted electron interaction in the

Co-N bonds, which may be in favor of the rapid dehydrogenation during HzOR [53]. The P-H bond strength for the CoP to CoPy is also quantified through the ICOHP. The corresponding ICOHP values are calculated to be  $-2.25$  and  $-0.17$  eV for CoP and CoPy, respectively. Relative to that for CoP, the occupation of antibonding states for CoPy quantitatively decreases, representing the weakened P-H bond strength on the CoPy surface, which is expected to obtain the moderate H\* adsorption energy.

### 3.4. Evaluation of OHzS performance

Given the excellent catalytic activity and stability of CoH-CoPy@CFP for both HzOR and HER, it can be used as not only the anode but also the cathode in overall hydrazine splitting (OHzS) electrolyzer (Fig. 5a). The 1.0 M KOH + 0.4 M N<sub>2</sub>H<sub>4</sub> and 1.0 M KOH are utilized as the electrolyte in anodic and cathodic rooms, respectively. As shown in Figs. 5b and 5c, the lab-scale OHzS electrolyzer assembled with CoH-CoPy@CFP (+, -) exhibits the cell voltages of 0.021, 0.045 and 0.088 V at the current densities of 50, 100, and 200 mA cm<sup>-2</sup>, respectively, which are much lower than the conventional overall water splitting (OWS) electrolyzer (1.662, 1.722 and 1.802 V) at the same current densities, suggesting the significant thermodynamic advantages for hydrazine-assisted H<sub>2</sub> production [54]. Notably, it requires an overpotential of only 0.23 V at industrial-grade large current density of 500 mA cm<sup>-2</sup>. Such a fascinating OHzS activity is also superior to those of CoCH-CoP@CFP, Pt/C@CFP, and the most recently published catalysts (Fig. 5d and Table S4). The electrochemical stability is assessed by accelerated cyclic voltammetry test, in which the current density of CoH-CoPy@CFP remains almost unchanged after 5000 cycles (Fig. S19). Meanwhile, the long-term durability has been further measured by the

chronoamperometric test at 100 mA cm<sup>-2</sup>, where the current density shows negligible decay after at least 100 h (Fig. 5e). Additionally, the volumes of generated N<sub>2</sub> and H<sub>2</sub> are measured by a conventional drainage method. Fig. 5f shows that the N<sub>2</sub>/H<sub>2</sub> volume ratios at different time points conform to the theoretical value of 2:1, [55] and the Faraday efficiencies of both anode and cathode are calculated to be nearly 100% with a H<sub>2</sub> production rate of 0.69 mL min<sup>-1</sup> cm<sup>-2</sup>. Such an excellent bifunctionality of CoH-CoPy@CFP can be attributed to two main factors: (i) Abundant electron-deficient Co sites on the reconstructed Co(OH)<sub>2</sub> phase form a powerful Co-N interaction for N<sub>2</sub>H<sub>4</sub> intermediates, which could accelerate the N<sub>2</sub>H<sub>4</sub> dehydrogenation kinetics. (ii) P vacancies are introduced into the HER-preferred CoP phase, which could balance the binding strength of H intermediates for obtaining a thermoneutral H\* absorption energy (Fig. 5g).

## 4. Conclusion

In summary, we propose a surface local-reconstruction strategy to integrate the CoP with rich P-vacancies and the Co(OH)<sub>2</sub> with electron-deficient Co sites into the CoH-CoPy@CFP catalyst, which possesses a bifunctional catalytic activity toward both HER and HzOR. This catalyst shows the outstanding catalytic performance featuring low overpotentials of  $-77$  and  $-130$  mV for HER as well as  $-61$  and  $-45$  mV for HzOR to reach 10 and 100 mA cm<sup>-2</sup>, superior to most reported non-noble metal catalysts. Besides, a lab-scale OHzS electrolyzer equipped with CoH-CoPy@CFP as both anode and cathode catalysts offers a cell voltage as low as 0.23 V to reach 500 mA cm<sup>-2</sup> for energy-saving H<sub>2</sub> production. The catalytic mechanism of HER/HzOR bifunctionality has been probed in-depth by DFT calculation. The P

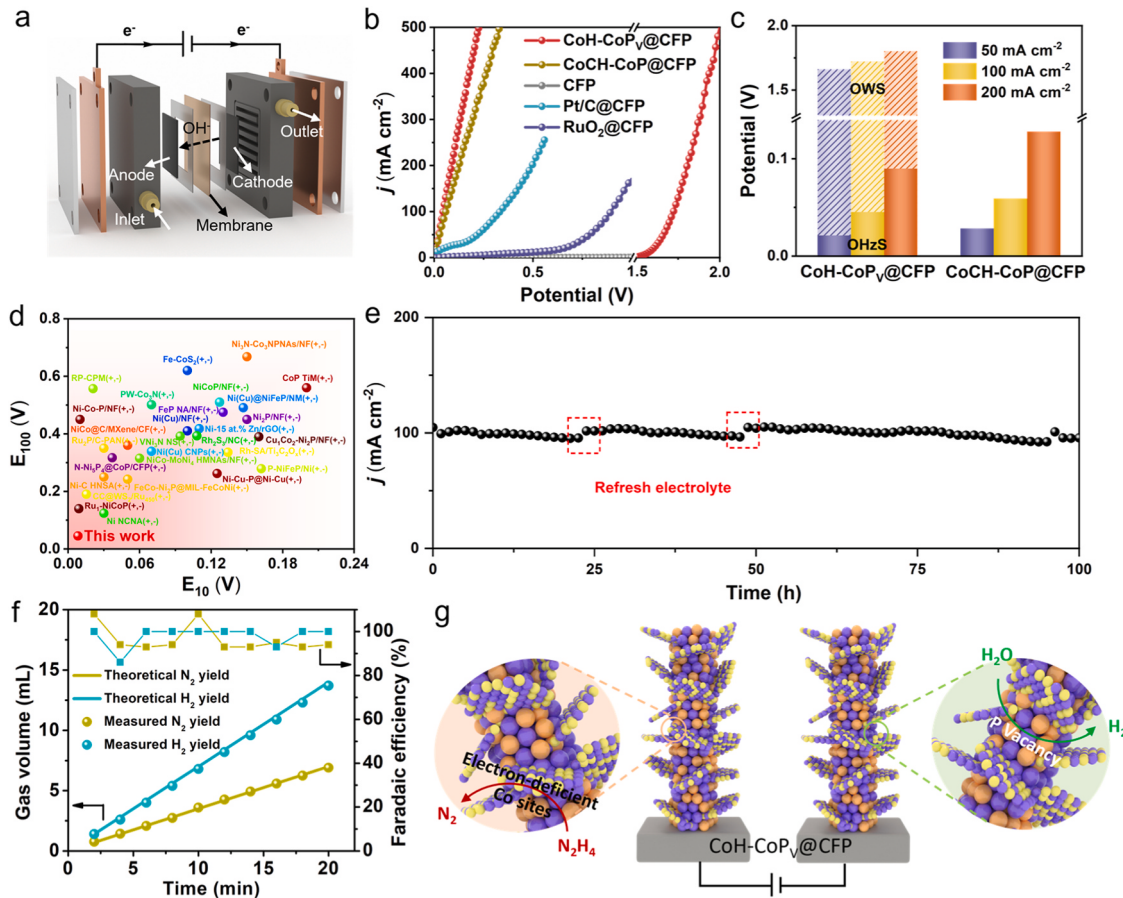


**Fig. 5.** (a) Schematic illustration of the lab-scale OHzS electrolyzer. (b) LSV curves, and (c) Comparison of the voltages required to achieve the current densities of 50, 100 and 200 mA cm<sup>-2</sup>. (d) Comparison of CoH-CoPy@CFP electrolyzer with the recently reported ones at 100 mA cm<sup>-2</sup>. (e) Chronoamperometric curve. (f) Hydrogen-yield rate and the corresponding Faraday efficiencies. (g) Schematic illustration of promotion mechanisms.

vacant CoP could create a thermoneutral H\* absorption value of 0.02 eV for enhancing HER activity, while Co(OH)<sub>2</sub> with electron-deficient Co sites exhibits a more favorable dehydrogenation ( ${}^*N_2H_4 \rightarrow {}^*N_2H_3$ ) kinetics benefiting from the powerful electron interaction between Co and N atoms. This work opens up a new avenue to construct the dual reactive sites towards HER and HzOR via a surface local-construction strategy that could guide the rational design of bifunctional catalysts.

### CRediT authorship contribution statement

**Wei Xiaotong:** Data curation, Investigation, Methodology, Validation, Writing – original draft. **Lv Xingshuai:** Data curation, Investigation, Methodology, Validation. **Zhang Shucong:** Conceptualization, Data curation, Investigation, Methodology, Writing – original draft. **Wang Huanlei:** Data curation, Supervision. **Dai Shuixing:** Data curation, Methodology. **Huang Minghua:** Conceptualization, Methodology, Resources, Supervision, Validation, Writing – review & editing.

### Declaration of Competing Interest

The authors declare that they have no known competing financial interests or personal relationships that could have appeared to influence the work reported in this paper.

### Data availability

Data will be made available on request.

### Acknowledgements

This work was financially supported by the National Natural Science Foundation of China (Nos. 22279124 and 52261145700), the Natural Science Foundation of Shandong Province (No. ZR2020ZD10), and the Fundamental Research Funds for the Central Universities (No. 202262010).

### Appendix A. Supporting information

Supplementary data associated with this article can be found in the online version at [doi:10.1016/j.apcatb.2023.123661](https://doi.org/10.1016/j.apcatb.2023.123661).

### References

- [1] J. Yang, A.R. Mohmad, Y. Wang, R. Fullon, X. Song, F. Zhao, I. Bozkurt, M. Augustin, E.J.G. Santos, H.S. Shin, W. Zhang, D. Voiry, H.Y. Jeong, M. Chhowalla, Ultrahigh-current-density niobium disulfide catalysts for hydrogen evolution, *Nat. Mater.* 18 (2019) 1309, <https://doi.org/10.1038/s41563-019-0463-8>.
- [2] J. Zhang, Y. Zhao, X. Guo, C. Chen, C.-L. Dong, R.-S. Liu, C.-P. Han, Y. Li, Y. Gogotsi, G. Wang, Single platinum atoms immobilized on an MXene as an efficient catalyst for the hydrogen evolution reaction, *Nat. Catal.* 1 (2018) 985, <https://doi.org/10.1038/s41929-018-0195-1>.
- [3] C.-T. Dinh, A. Jain, F.P.G. de Arquer, P. De Luna, J. Li, N. Wang, X. Zheng, J. Cai, B. Z. Gregory, O. Voznyy, B. Zhang, M. Liu, D. Sinton, E.J. Crumlin, E.H. Sargent, Multi-site electrocatalysts for hydrogen evolution in neutral media by destabilization of water molecules, *Nat. Energy* 4 (2018) 107, <https://doi.org/10.1038/s41560-018-0296-8>.
- [4] W. Tong, M. Forster, F. Dionigi, S. Dresp, R. Sadeghi Erami, P. Strasser, A.J. Cowan, P. Farràs, Electrolysis of low-grade and saline surface water, *Nat. Energy* 5 (2020) 367–377, <https://doi.org/10.1038/s41560-020-0550-8>.
- [5] J. Guo, Y. Zheng, Z. Hu, C. Zheng, J. Mao, K. Du, M. Jaroniec, S.-Z. Qiao, T. Ling, Direct seawater electrolysis by adjusting the local reaction environment of a catalyst, *Nat. Energy* 8 (2023) 264–272, <https://doi.org/10.1038/s41560-023-01195-x>.
- [6] S. Chen, S. Zhang, L. Guo, L. Pan, C. Shi, X. Zhang, Z.F. Huang, G. Yang, J.J. Zou, Reconstructed Ir-O-Mo species with strong Brønsted acidity for acidic water oxidation, *Nat. Commun.* 14 (2023) 4127, <https://doi.org/10.1038/s41467-023-39822-6>.
- [7] Y. Wu, Y. Zhao, P. Zhai, C. Wang, J. Gao, L. Sun, J. Hou, Triggering lattice oxygen activation of single-atomic Mo sites anchored on Ni-Fe oxyhydroxides nanoarrays for electrochemical water oxidation, *Adv. Mater.* 34 (2022) 2202523, <https://doi.org/10.1002/adma.202202523>.
- [8] Q. Qian, J. Zhang, J. Li, Y. Li, X. Jin, Y. Zhu, Y. Liu, Z. Li, A. El-Harairy, C. Xiao, G. Zhang, Y. Xie, Artificial heterointerfaces achieve delicate reaction kinetics towards hydrogen evolution and hydrazine oxidation catalysis, *Angew. Chem. Int. Ed.* 60 (2021) 5984, <https://doi.org/10.1002/anie.202014362>.
- [9] Z. Wang, L. Xu, F. Huang, L. Qu, J. Li, K.A. Owusu, Z. Liu, Z. Lin, B. Xiang, X. Liu, K. Zhao, X. Liao, W. Yang, Y.-B. Cheng, L. Mai, Copper-nickel nitride nanosheets as efficient bifunctional catalysts for hydrazine-assisted electrolytic hydrogen production 9 (2019) 1900390, <https://doi.org/10.1002/aenm.201900390>.
- [10] F. Sun, J. Qin, Z. Wang, M. Yu, X. Wu, X. Sun, J. Qiu, Energy-saving hydrogen production by chlorine-free hybrid seawater splitting coupling hydrazine degradation, *Nat. Commun.* 12 (2021) 4182, <https://doi.org/10.1038/s41467-021-24529-3>.
- [11] Y. Zhang, L. Gao, S. Ma, T. Hu, A multifunctional metal-organic framework with a  $\mu$ 3-OH site for gas and vapor sorption and selective detection of nitrofurantoin, *J. Mater. Chem. C* 10 (2022) 1136–1143, <https://doi.org/10.1039/DTC04482F>.
- [12] C. Feng, M. Lyu, J. Shao, H. Wu, W. Zhou, S. Qi, C. Deng, X. Chai, H. Yang, Q. Hu, C. He, Lattice strain engineering of Ni<sub>3</sub>P enables efficient catalytic hydrazine oxidation-assisted hydrogen production, *Adv. Mater.* 35 (2023) 2305598, <https://doi.org/10.1002/adma.202305598>.
- [13] Y. Liu, J. Zhang, Y. Li, Q. Qian, Z. Li, G. Zhang, Realizing the synergy of interface engineering and chemical substitution for Ni<sub>3</sub>N enables its bifunctionality toward hydrazine oxidation assisted energy-saving hydrogen production, *Adv. Funct. Mater.* 31 (2021) 2103673, <https://doi.org/10.1002/adfm.202103673>.
- [14] Y. Liu, J. Zhang, Y. Li, Q. Qian, Z. Li, G. Zhang, Manipulating dehydrogenation kinetics through dual-doping Co<sub>3</sub>N electrode enables highly efficient hydrazine oxidation assisting self-powered H<sub>2</sub> production, *Nat. Commun.* 11 (2020) 1853, <https://doi.org/10.1038/s41467-020-15563-8>.
- [15] Y. Li, J. Li, Q. Qian, X. Jin, Y. Liu, Z. Li, Y. Zhu, Y. Guo, G. Zhang, Superhydrophilic Ni-based multicomponent nanorod-confined-nanoflake array electrode achieves waste-battery-driven hydrogen evolution and hydrazine oxidation, *Small* 17 (2021) 2008148, <https://doi.org/10.1002/smll.202008148>.
- [16] A.O. Elnabawy, J.A. Herron, S. Karraker, M. Mavrikakis, Structure sensitivity of ammonia electro-oxidation on transition metal surfaces: a first-principles study, *J. Catal.* 397 (2021) 137–147, <https://doi.org/10.1016/j.jcat.2021.03.010>.
- [17] H. Yang, P. Guo, R. Wang, Z. Chen, H. Xu, H. Pan, D. Sun, F. Fang, R. Wu, Sequential phase conversion-induced phosphides heteronanorod arrays for superior hydrogen evolution performance to Pt in wide pH media, *Adv. Mater.* 34 (2022) 2107548, <https://doi.org/10.1002/adma.202107548>.
- [18] S. Zhang, C. Zhang, X. Zheng, G. Su, H. Wang, M. Huang, Integrating electrophilic and nucleophilic dual sites on heterogeneous bimetallic phosphide via enhancing interfacial electronic field to boost hydrazine oxidation and hydrogen evolution, *Appl. Catal. B Environ.* 324 (2023) 122207, <https://doi.org/10.1016/j.apcatb.2022.122207>.
- [19] S. Zhou, Y. Zhao, R. Shi, Y. Wang, A. Ashok, F. Heraly, T. Zhang, J. Yuan, Vacancy-rich MXene-immobilized Ni single atoms as a high-performance electrocatalyst for the hydrazine oxidation reaction, *Adv. Mater.* 34 (2022) 2204388, <https://doi.org/10.1002/adma.202204388>.
- [20] Y. Hu, T. Chao, Y. Li, P. Liu, T. Zhao, G. Yu, C. Chen, X. Liang, H. Jin, S. Niu, W. Chen, D. Wang, Y. Li, Cooperative Ni(Co)-Ru-P sites activate dehydrogenation for hydrazine oxidation assisting self-powered H<sub>2</sub> production, *Angew. Chem. Int. Ed.* 62 (2023) e202308800, <https://doi.org/10.1002/anie.202308800>.
- [21] Y. Yang, X. Li, G. Liu, H. Liu, Y. Shi, C. Ye, Z. Fang, M. Ye, J. Shen, Hierarchical Ohmic contact interface engineering for efficient hydrazine-assisted hydrogen evolution reaction, *Adv. Mater.* (2023), <https://doi.org/10.1002/adma.202307979>.
- [22] J. Yang, W. Li, D. Wang, Y. Li, Electronic metal-support interaction of single-atom catalysts and applications in electrocatalysis, *Adv. Mater.* 32 (2020) 2003300, <https://doi.org/10.1002/adma.202003300>.
- [23] X. Zhao, M. Liu, Y. Wang, Y. Xiong, P. Yang, J. Qin, X. Xiong, Y. Lei, Designing a built-in electric field for efficient energy electrocatalysis, *ACS Nano* 16 (2022) 19959–19979, <https://doi.org/10.1021/acsnano.2c09888>.
- [24] S. Zhang, C. Tan, R. Yan, X. Zou, F.L. Hu, Y. Mi, C. Yan, S. Zhao, Constructing built-in electric field in heterogeneous nanowire arrays for efficient overall water electrolysis, *Angew. Chem. Int. Ed.* 62 (2023) e202302795, <https://doi.org/10.1002/anie.202302795>.
- [25] S. Zhao, Y. Yang, Z. Tang, Insight into structural evolution, active sites, and stability of heterogeneous electrocatalysts, *Angew. Chem. Int. Ed.* 61 (2022) e202110186, <https://doi.org/10.1002/anie.202110186>.
- [26] C. Huang, Q. Zhou, D. Duan, L. Yu, W. Zhang, Z. Wang, J. Liu, B. Peng, P. An, J. Zhang, L. Li, J. Yu, Y. Yu, The rapid self-reconstruction of Fe-modified Ni hydroxysulfide for efficient and stable large-current-density water/seawater oxidation, *Energy Environ. Sci.* 15 (2022) 4647–4658, <https://doi.org/10.1039/D2EE01478E>.
- [27] C. Yang, W. Zhong, K. Shen, Q. Zhang, R. Zhao, H. Xiang, J. Wu, X. Li, N. Yang, Electrochemically reconstructed Cu-FeOOH/Fe<sub>3</sub>O<sub>4</sub> catalyst for efficient hydrogen evolution in alkaline media, *Adv. Energy Mater.* 12 (2022) 2200077, <https://doi.org/10.1002/aenm.202200077>.
- [28] P. Bhojane, A. Le Bail, P.M. Shirage, A quarter of a century after its synthesis and with >200 papers based on its use, 'Co(CO<sub>3</sub>)<sub>0.5</sub>(OH)<sub>0.11</sub>H<sub>2</sub>O' proves to be Co<sub>6</sub>(CO<sub>3</sub>)<sub>2</sub>(OH)<sub>8</sub>·H<sub>2</sub>O from synchrotron powder diffraction data, *Acta Cryst., C75* (2019) 61–64. <https://doi.org/10.1107/S2053229618017734>.
- [29] X. Leng, L. Wu, Y. Liu, C. Li, S. Wei, Z. Jiang, G. Wang, J. Lian, Q. Jiang, A novel open architecture built by ultra-fine single-crystal Co<sub>2</sub>(CO<sub>3</sub>)(OH)<sub>2</sub> nanowires and reduced graphene oxide for asymmetric supercapacitors, *J. Mater. Chem. A* 4 (2016) 17171, <https://doi.org/10.1039/C6TA07112K>.

[30] X. Tan, S. Geng, Y. Ji, Q. Shao, T. Zhu, P. Wang, Y. Li, X. Huang, Closest packing polymorphism interfaced metastable transition metal for efficient hydrogen evolution, *Adv. Mater.* 32 (2020) 2002857, <https://doi.org/10.1002/adma.202002857>.

[31] K.R. Yoon, K. Shin, J. Park, S.H. Cho, C. Kim, J.W. Jung, J.Y. Cheong, H.R. Byon, H. M. Lee, I.D. Kim, Brush-like cobalt nitride anchored carbon nanofiber membrane: current collector-catalyst integrated cathode for long cycle Li-O<sub>2</sub> batteries, *ACS Nano* 12 (2018) 128–139, <https://doi.org/10.1021/acsnano.7b03794>.

[32] Z. Lv, W. Ma, M. Wang, J. Dang, K. Jian, D. Liu, D. Huang, Co-constructing interfaces of multiheterostructure on MXene (Ti<sub>3</sub>C<sub>2</sub>T<sub>x</sub>)-modified 3D self-supporting electrode for ultraefficient electrocatalytic HER in alkaline media, *Adv. Funct. Mater.* 31 (2021) 2102576, <https://doi.org/10.1002/adfm.202102576>.

[33] G. Yuan, J. Bai, L. Zhang, X. Chen, L. Ren, The effect of P vacancies on the activity of cobalt phosphide nanorods as oxygen evolution electrocatalyst in alkali, *Appl. Catal. B Environ.* 284 (2021) 119693, <https://doi.org/10.1016/j.apcatb.2020.119693>.

[34] X. Li, Q. Hu, H. Wang, M. Chen, X. Hao, Y. Ma, J. Liu, K. Tang, A. Abudula, G. Guan, Charge induced crystal distortion and morphology remodeling: Formation of Mn-CoP nanowire @ Mn-CoOOH nanosheet electrocatalyst with rich edge dislocation defects, *Appl. Catal. B Environ.* 292 (2021) 120172, <https://doi.org/10.1016/j.apcatb.2021.120172>.

[35] X. Shan, J. Liu, H. Mu, Y. Xiao, B. Mei, W. Liu, G. Lin, Z. Jiang, L. Wen, L. Jiang, An engineered superhydrophilic/superaerophobic electrocatalyst composed of the supported CoMoS<sub>x</sub> chalcogel for overall water splitting, *Angew. Chem. Int. Ed.* 59 (2020) 1659–1665, <https://doi.org/10.1002/anie.201911617>.

[36] S. Zhang, W. Wang, F. Hu, Y. Mi, S. Wang, Y. Liu, X. Ai, J. Fang, H. Li, T. Zhai, 2D CoOOH sheet-encapsulated Ni<sub>2</sub>P into tubular arrays realizing 1000 mA cm<sup>-2</sup>-level-current-density hydrogen evolution over 100h in neutral water, *Nano Micro Lett.* 12 (2020) 140, <https://doi.org/10.1007/s40820-020-00476-4>.

[37] Y. Wang, L. Yan, K. Dastafkan, C. Zhao, X. Zhao, Y. Xue, J. Huo, S. Li, Q. Zhai, Lattice matching growth of conductive hierarchical porous MOF/LDH heteronanotube arrays for highly efficient water oxidation, *Adv. Mater.* 33 (2021) 2006351, <https://doi.org/10.1002/adma.202006351>.

[38] T. Deng, Y. Lu, W. Zhang, M. Sui, X. Shi, D. Wang, W. Zheng, Inverted design for high-performance supercapacitor via Co(OH)<sub>2</sub>-derived highly oriented MOF electrodes, *Adv. Energy Mater.* 8 (2018) 1702294, <https://doi.org/10.1002/aenm.201702294>.

[39] Q. Zhou, Z. Shen, C. Zhu, J. Li, Z. Ding, P. Wang, F. Pan, Z. Zhang, H. Ma, S. Wang, H. Zhang, Nitrogen-doped CoP electrocatalysts for coupled hydrogen evolution and sulfur generation with low energy consumption, *Adv. Mater.* 30 (2018) 1800140, <https://doi.org/10.1002/adma.201800140>.

[40] C. Liang, P. Zou, A. Nairan, Y. Zhang, J. Liu, K. Liu, S. Hu, F. Kang, H.J. Fan, C. Yang, Exceptional performance of hierarchical Ni-Fe oxyhydroxide@NiFe alloy nanowire array electrocatalysts for large current density water splitting, *Energy Environ. Sci.* 13 (2020) 86–95, <https://doi.org/10.1039/C9EE02388G>.

[41] R. Wu, B. Xiao, Q. Gao, Y.-R. Zheng, X.-S. Zheng, J.-F. Zhu, M.R. Gao, S.-H. Yu, A Janus nickel cobalt phosphide catalyst for high-efficiency neutral-pH water splitting, *Angew. Chem.* 130 (2018) 15671–15675, <https://doi.org/10.1002/ange.201808929>.

[42] H. Zhang, Y. Zhou, M. Xu, A. Chen, Z. Ni, O. Akdim, T. Wagberg, X. Huang, G. Hu, Interface engineering on amorphous/crystalline hydroxides/sulfides heterostructure nanoarrays for enhanced solar water splitting, *ACS Nano* 17 (2023) 636–647, <https://doi.org/10.1021/acsnano.2c09880>.

[43] Z. Chang, G. Meng, Y. Chen, C. Chen, S. Han, P. Wu, L. Zhu, H. Tian, F. Kong, M. Wang, X. Cui, J. Shi, Dual-site W-O-CoP catalysts for active and selective nitrate conversion to ammonia in a broad concentration window, *Adv. Mater.* 35 (2023) 2304508, <https://doi.org/10.1002/adma.202304508>.

[44] L. Bai, Z. Hu, C. Hu, S. Zhang, Y. Ying, Y. Zhang, L. Li, H. Zhang, N. Li, S. Shi, S. Liu, L. Hao, T. Liu, H. Huang, H. Huang, Y. Zhang, Utilizing cationic vacancies and spontaneous polarization on cathode to enhance zinc-ion storage and inhibit dendrite growth in zinc-ion batteries, *Angew. Chem. Int. Ed.* 62 (2023) e202301631, <https://doi.org/10.1002/anie.202301631>.

[45] T. Wang, X. Cao, L. Jiao, Progress in hydrogen production coupled with electrochemical oxidation of small molecules, *Angew. Chem. Int. Ed.* 61 (2022) e202213328, <https://doi.org/10.1002/anie.202213328>.

[46] J. Zhou, Z. Han, X. Wang, H. Gai, Z. Chen, T. Guo, X. Hou, L. Xu, X. Hu, M. Huang, S.V. Levchenko, H. Jiang, Discovery of quantitative electronic structure-OER activity relationship in metal-organic framework electrocatalysts using an integrated theoretical-experimental approach, *Adv. Funct. Mater.* 31 (2021) 2102066, <https://doi.org/10.1002/adfm.202102066>.

[47] D. Yu, Y. Hao, S. Han, S. Zhao, Q. Zhou, C.H. Kuo, F. Hu, L. Li, H.Y. Chen, J. Ren, S. Peng, Ultrafast combustion synthesis of robust and efficient electrocatalysts for high-current-density water oxidation, *ACS Nano* 17 (2023) 1701–1712, <https://doi.org/10.1021/acsnano.2c11939>.

[48] X. Wang, X. Zhou, C. Li, H. Yao, C. Zhang, J. Zhou, R. Xu, L. Chu, H. Wang, M. Gu, H. Jiang, M. Huang, Asymmetric Co-N<sub>3</sub>P<sub>1</sub> trifunctional catalyst with tailored electronic structures enabling boosted activities and corrosion resistance in an uninterrupted seawater splitting system, *Adv. Mater.* 34 (2022) 2204021, <https://doi.org/10.1002/adma.202204021>.

[49] X. Xu, T. Wang, W. Lu, L. Dong, H. Zhang, X. Miao, Co<sub>x</sub>P@Co<sub>3</sub>O<sub>4</sub> Nanocomposite on cobalt foam as efficient bifunctional electrocatalysts for hydrazine-assisted hydrogen production, *ACS Sustain. Chem. Eng.* 9 (2021) 4688–4701, <https://doi.org/10.1021/acsschemeng.1c00705>.

[50] Q. Wen, J. Duan, W. Wang, D. Huang, Y. Liu, Y. Shi, J. Fang, A. Nie, H. Li, T. Zhai, Engineering a local free water enriched microenvironment for surpassing platinum hydrogen evolution activity, *Angew. Chem. Int. Ed.* 61 (2022) e202206077, <https://doi.org/10.1002/anie.202206077>.

[51] W. Wang, Z. Wang, R. Yang, J. Duan, Y. Liu, A. Nie, H. Li, B.Y. Xia, T. Zhai, In situ phase separation into coupled interfaces for promoting CO<sub>2</sub> electroreduction to formate over a wide potential window, *Angew. Chem. Int. Ed.* 60 (2021) 22940–22947, <https://doi.org/10.1002/anie.202110000>.

[52] X. Wang, S. Li, Z. Yuan, Y. Sun, Z. Tang, X. Gao, H. Zhang, J. Li, S. Wang, D. Yang, J. Xie, Z. Yang, Y.M. Yan, Optimizing electrocatalytic nitrogen reduction via interfacial electric field modulation: elevating d-band center in WS<sub>2</sub>-WO<sub>3</sub> for enhanced intermediate adsorption, *Angew. Chem. Int. Ed.* 62 (2023) e202303794, <https://doi.org/10.1002/anie.202303794>.

[53] N. Wen, D. Zhang, X. Zhao, X. Jiao, Y. Xia, D. Chen, Polarization manipulation of NiO nanosheets engineered with Fe/Pt single atoms for high-performance electrocatalytic overall alkaline seawater splitting, *ACS Catal.* 13 (2023) 7868–7878, <https://doi.org/10.1021/acscatal.3c01101>.

[54] G.B. Darband, M. Maleki, A. Toghraei, S. Shammugam, Electrodeposition of self-supported transition metal phosphides nanosheets as efficient hydrazine-assisted electrolytic hydrogen production catalyst, *Int. J. Hydrol. Energy* 48 (2023) 4253–4263, <https://doi.org/10.1016/j.ijhydene.2022.10.246>.

[55] R. Guo, L. Gao, Y. Zhang, X. Zhang, M. Ma, T. Hu, Enhancing hydrazine-assisted hydrogen production by constructing CoP-Co<sub>2</sub>P bifunctional catalysts, *Appl. Surf. Sci.* 617 (2023) 156602, <https://doi.org/10.1016/j.apsusc.2023.156602>.